IEEE Access
Multidisciplinary | Rapid Review | Open Access Journal

Received April 7, 2019, accepted May 3, 2019, date of publication May 7, 2019, date of current version May 20, 2019.

Digital Object Identifier 10.1109/ACCESS.2019.2915169

Automatic Counting and Individual Size and Mass Estimation of Olive-Fruits Through Computer Vision Techniques

JUAN M. PONCE, ARTURO AQUINO, BORJA MILLAN, AND JOSÉ M. ANDÚJAR, (Senior Member, IEEE)
Department of Electronic Engineering, Computer Systems and Automation, University of Huelva, 21819 Huelva, Spain

Corresponding author: Juan M. Ponce (jmponce.real@diesia.uhu.es)

This work and APC were supported in part by the INTERREG Cooperation Program V-A SPAIN-PORTUGAL (POCTEP) 2014–2020, and in part by the ERDF funds under Grant 0155_TECNOLIVO_6_E, within the scope of the TecnOlivo Project.

ABSTRACT Fruit grading is an essential post-harvest task in the olive industry, where size-and-mass based fruit classification is especially important when processing high-quality table olives. Within this context, this research presents a new methodology aimed at supporting accurate automatic olive-fruit grading by using computer vision techniques and feature modeling. For its development, a total of 3600 olive-fruits from nine varieties were photographed, stochastically distributing the individuals on the scene, using an ad-hoc designed an imaging chamber. Then, an image analysis algorithm, based on mathematical morphology, was designed to individually segment olives and extract descriptive features to estimate their major and minor axes and their mass. Regarding its accuracy for the individual segmentation of olive-fruits, the algorithm was proven through 117 captures containing 11 606 fruits, producing only six fruit-segmentation mistakes. Furthermore, by linearly correlating the data obtained by image analysis and the corresponding reference measurements, models for estimating the three features were computed. Then, the models were tested on 2700 external validation samples, giving relative errors below 0.80% and 1.05% for the estimation of the major and minor axis length for all varieties, respectively. In the case of estimating olive-fruit mass, the models provided relative errors never exceeding 1.16%. The ability of the developed algorithm to individually segment olives stochastically positioned, along with the low error rates of around 1% reported by the estimation models for the three features, makes the methodology a promising alternative to be integrated into a new generation of improved and non-invasive olive classification machines. The new developed system has been registered in the Spanish Patent and Trademark Office with the number P201930297.

INDEX TERMS Computer vision, feature modeling, food industry, fruit grading, image analysis, olive.

I. INTRODUCTION

The olive (Olea europaea) is a species belonging to the family of Oleaceae, which nowadays comprises one of the most significative horticultural crops worldwide. Mainly due to the increase of popularity the olive-derived products have experienced over the last decades, its cultivation, practiced for centuries in the Mediterranean Basin, has spread all around the world. Indeed, it can be found with a growing presence in such disparate countries as China, Australia or USA [1], [2]. This geographical expansion has obviously been accompanied by a huge growth in terms of production, which is directly reflected in the numbers the olive industry deals with. Thus, according to estimations for the 2018/19 crop year, a table olive production of 2,750,000 tons [3], and 3,130,000 tons for the case of olive oil is expected [4].

The increasing demand and consumption of these olive-based products has led the industry to explore the use of new technologies aimed at developing a more profitable, competitive and sustainable market around it. Thus, as in other mainstream crops, olive sector is currently experiencing a process of major transformation [5], [6].

When talking about table olives, fruit classification according to size is a relevant task undertaken during postharvest manufacturing [7]. Size homogeneity, along with other

The associate editor coordinating the review of this manuscript and approving it for publication was Carmelo Militello.

sensory attributes, have a positive impact on the overall consumer opinion about the quality of the product [8]. Furthermore, this is not exclusive of olives, since fruit-size grading is a global issue within food industry when processing high-quality horticultural commodities [9]. So much so that its automation has been historically a challenge to deal with, since this activity has traditionally been performed by hand, with all the drawbacks that it brings. First approaches to the problem have been based on purely mechanical solutions, as the integration of different size hoppers through which fruits can slide, according to their dimensions, into the conveyor belts used during postharvest treatment. However, they can potentially damage fruits [10], [11], since it implies a higher degree of physical manipulation of the commodities. In addition, they present obvious limitations in terms of the features the classification can be based on, and the information that can be recorded after processing.

Within the described scenario, the classical mechanical approaches have been reviewed in recent years [12], being machine vision probably the most investigated technique to build a new generation of less invasive postharvest horticultural classification machines. Thus, Baigvand et al. [13] proposed a machine-vision-based integral solution for dried figs sorting. Sad et al. [14] presented a methodology fusing image processing and supervised machine learning for grading mangoes according to shape and mass. Focused on the same crop, Wang et al. [15] suggested the use of RGB-D sensing for in-field fruit size estimation. In addition, Mizushima and Lu [16] faced the segmentation of images of apples, in order to enable their automatic sorting.

Likewise, the use of computer vision techniques has already been approached within the olive sector. Gatica et al. [17] proposed RGB-image analysis and the use of neural networks to recognize the fruits directly in the trees, thus ideally estimating the best harvest time. On the other hand, several studies have focused on varietal identification on the basis of image analysis. Thus, Martínez et al. [18] approached the problem by feature extraction from images of olive endocarps, and then using partial least square-discriminant classifiers. Similarly, the proposal by Beyaz et al. [19] used captures of fruits and endocarps to identify olive cultivars. Aside from variety classification, research has also been conducted to deal with defective fruit discrimination. To this effect, Diaz et al. [20] compared different algorithms for categorizing olives according to their surface condition. On the other hand, Puerto et al. [21] presented a methodology for differentiating olives collected from the ground from those harvested directly from the trees, as the former impoverishes quality of the subsequently produced olive oil.

In a previous research, Ponce et al. [22] successfully found strong evidences about the viability of the estimation of mass and size of olives by means of image analysis. In order to extend the scope approached then, a highly improved new methodology, based on computer vision and feature modelling, is proposed in the present paper. It undertakes a new scenario, closer to match the needs of the olive industry in terms of automated fruit grading. Thus, an image acquisition chamber, potentially integrable in a conveyor belt, was designed with the capability of taking photos of olive batches under controlled conditions. With this device, groups of olives from nine different varieties were photographed, stochastically positioning the individuals on the capturing area to mimic the chaotic distribution they would have on real a conveyor belt. Then, the images were binarized by clustering-based image thresholding, and the olives appearing fused for being in touch were separated employing mathematical morphology principles. After isolating the individual olives, descriptive data of the features under study were extracted from the transformed images. Finally, a linear regression analysis of the correlation between these measurements and their corresponding individual objective observations, previously taken in laboratory, was performed to compute the models for estimating size and mass of every single olive appearing in images.

Unlike other studies in this field, the methodology presented is novel because, in the first place, it proposes a specific image acquisition system, designed to favor binarization of the captures with high precision, at a low computational cost. It makes possible to face the subsequent individual segmentation of the fruits within a timeframe potentially assumable to be applicable in a real time system, with the implications that this entails in terms of usability for the olive industry. In addition, the significant volume of samples used during the development of the study offers guarantees of the reliability and generality of the results obtained.

Hereafter, the manuscript is divided into three main parts. First, section II focuses on the experimental design, presenting different aspects related to the characteristics of those fruit- samples used throughout the research (section II-A), describing how the image acquisition and reference data collection (section II-B) was carried out, and detailing the framework whereby the image analysis algorithm was developed (section II-C). Section III offers insights into the developed methodology, laying emphasis on how this image analysis procedure was designed to binarize (section III-A), segment at fruit-level (section III-B), and postprocess the initial captures (section III-C). Next, feature characterization (section III-D) and modelling (III-E) are addressed, and methodology's performance evaluation is detailed (section III-F). In section IV, the results attained are presented and discussed. Finally, the last section summarizes the findings achieved, and formulates the main conclusions derived from the present study.

II. MATERIALS AND METHODS

A. SAMPLE COLLECTION

Nine Olea europaea varieties were considered for this study: Arbequina, Arbosana, Picual, Ocal, Changlot Real, Verdial de Huévar, Lechín de Sevilla and two experimental ones, named as 967 and 1030, respectively. Thus, 400 samples per variety (3,600 in total) were gathered by hand in olive

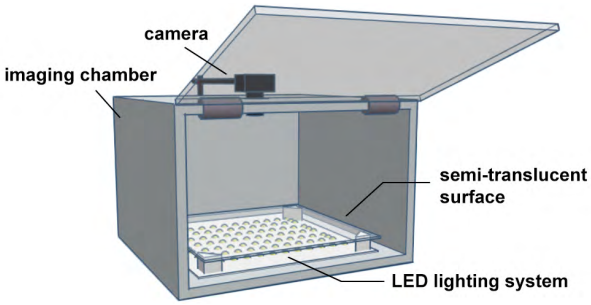

FIGURE 1. Image acquisition chamber.

orchards located in Gibraleón (37°20′09.2″N 7°02′19.8″W), province of Huelva (Andalusia, Spain), in October 2018. For each variety, samples were selected to cover the observed variability in terms of size.

B. REFERENCE DATA AND IMAGE ACQUISITION

For image capture, an imaging chamber was designed and crafted with the aim of isolating the scene from any external light source, thus maximizing illumination control (see Fig. 1).

The fruits were placed on a semi translucent white plastic sheet. This sheet, with dimensions of 500 × 500 × 2 mm, was neatly disposed 65 mm from the bottom of the chamber, and it was illuminated from below by a set of seven equally distributed strips composed of 25 LEDs of 5V each. Due to this lighting system design, it was possible to avoid shadows cast by the fruits. As capturing device, a Sony α7-II digital mirrorless camera (Sony Corp., Tokyo, Japan) was installed at the top of the chamber, looking perpendicularly at the imaging area. The camera mounted a 24 Mpx CCD stabilized sensor, and it was equipped with a Zeiss 24/70mm lens with optical stabilization. It was set in manual mode, configuring the aperture in f/7.1, shutter speed in 1/50s, ISO sensitivity in 250, and focal length in 31mm. The camera was set to save images in JPEG file format, with a 6000 × 3376-pixel resolution, a color-depth of 24 bits, and a pixel density of 350 ppi.

Every variety set of 400 olives was divided into batches of 50 fruits, which were then photographed separately, thus obtaining eight images per variety (72 in total). The only criterion regarding to the way the fruits where disposed to be imaged, was to force multiple touching occurrences. This prerequisite was established with the purpose of approaching a complex and realistic scenario.

Additionally, in order to test the robustness and accuracy of the developed image analysis algorithm, a set of five stress-images were acquired per variety (45 in total). The number of fruits to appear was progressively incremented in each of these five images. Two examples of the images acquired can be checked in Figure 2. Furthermore, Table 1 summarizes how the olive-fruit samples were organized and photographed for the nine studied varieties.

Once a batch was photographed, measurements of mass and size were conducted and registered for every individual fruit. To do so, a KERN PCB 3500-2 precision balance (KERN & Sohn GmbH, Balingen, Germany) was used to assess olive mass (in grams - g). To grade the size of each fruit, its corresponding major and minor axis length were measured (in millimeters - mm) using a Digital Vernier Caliper, which provided 0.01mm of resolution and 0.02mm of accuracy. It must be pointed out that, for every variety, the major and minor axes of 100 of the 400 individuals (900 in total), were independently measured by three different observers, again manually by using a digital caliper. This, in order to later perform a study of variability, with the goal of assessing the degree of uncertainty introduced by measuring the size of the olives by hand, using the digital caliper.

FIGURE 2. Examples of captured images for Picual variety: (a) regular image; (b) stress image.

TABLE 1. Materials: organization of olive-fruit samples and images for each of the nine varieties used.

	Olive fruits		Images acquired	
Variety sample	Training subset	External validation subset	Regular images	Stress images
400 (fruits)	100 (fruits)	300 (fruits)	8[a]	5[b]

[a] 50 fruits per image.
[b] Stochastic number of fruits.

C. IMAGE ANALYSIS ALGORITHM IMPLEMENTATION

The core of the proposed methodology is an image analysis algorithm designed in order to, first, transform the olive-fruit captures into binary-segmented images, and second, to extract from them data structures with which to perform fruit counting and characterization of the three different features to estimate. The latter, for each of the fruits that appear in the initial captures. Its development was carried out by mainly using transformations based on mathematical morphology, and binarization by statistical thresholding techniques. Regarding its implementation, MATLAB and the Image Processing Toolbox Release 2018a (The MathWorks, Inc., Natick, Massachusetts, USA) were used. To note this technology was chosen only for prototyping purposes, with the awareness that a real system, based on the proposed methodology, would require an algorithmic implementation based on a computationally more flexible and efficient language.

III. DEVELOPED METHODOLOGY

The diagram shown in Fig. 3 illustrates the methodology resulting from the conducted research. Essentially, the dataset

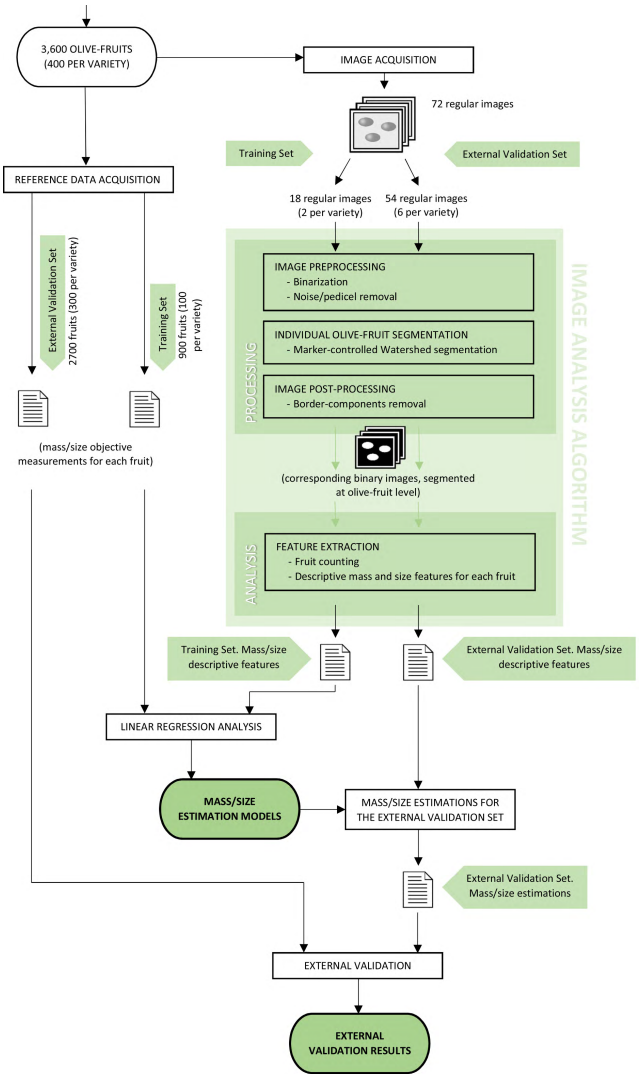

FIGURE 3. Representative diagram of the developed methodology for computing and validating the mass and size olive-fruits estimation models.

composed of the acquired olive-fruit images and their corresponding reference measurements, previously recorded, is used throughout an image processing and analysis procedure aimed at computing, and ultimately validating, the pursued models for fruit mass and size estimation. This process of transforming the captures and extracting descriptive features of fruits, to feed estimation model training, is described in detail throughout the subsections below.

A. IMAGE PREPROCESSING

As it has been stated before, the present study is focused on a scenario in which olives may appear in touch with other in the images. Within this context, the developed image analysis algorithm was designed on the basis of the Watershed transform [23] for individually segmenting olive-fruits. This section describes a set of image transformations applied to favor the performance of this subsequent Watershed transform application.

First, an image binarization consisting in isolating those pixels corresponding to fruits from the background is carried out. To that end, images are previously transformed from RGB to HSV color space [24]. A large body of literature has investigated the importance of using the right color representation when developing image analysis procedures, with no exception when treating captures of horticultural products, whatever the pursued objectives are [25], [26]. In the present study, the specific illumination conditions enabled the acquisition of images with an important differentiation, in terms of luminosity or brightness, between the background-pixels and the fruits. In order to exploit this feature to the purpose of binarizing the image, HSV comprises a suitable color representation, since brightness information can be directly analyzed in the specific channel V (Value). Thus, for its processing, this channel is treated as a grayscale image, denoted as I_V, and its grey-level values are inverted to represent background pixels with lower values than those of fruits:

$$\bar{I_V} = 255 - I_V \tag{1}$$

where 255 is the highest possible grey-level value for images with 8 bits-per-channel of color depth. Then, $\bar{I_V}$ is binarized based on a threshold computed by Otsu's method [27]. This global thresholding technique assumes that there are two classes of pixels in terms of their grey-level values, those belonging to the foreground and those which correspond to the background. Thus, the method automatically calculates the optimum threshold for class separation by maximizing the inter-class variance or, analogously, by minimizing the intra-class variance, so the sum of the measured spreads of the pixel levels of both classes is minimum. Hence, the threshold Th_{Otsu} is computed for image $\bar{I_V}$, which is then binarized as:

$$I_{Bin}(x, y) = \begin{cases} 255 & if\ \bar{I_V}\ (x, y) > Th_{Otsu} \\ 0 & in\ any\ other\ case \end{cases} \tag{2}$$

Next, a morphological opening is applied to the resulting binary image with a double purpose: 1) to eliminate tiny groups of white pixels which cannot represent olives because of their anomalous dimensions; 2) to remove the olive pedicels that might be present in the image. Mathematically:

$$I_{Bin2} = \gamma_\beta\ (I_{Bin})\ , \tag{3}$$

where γ is the morphological opening that uses the disk-shaped structuring element β of 30 pixels in radio [23, pp. 106-108]. This process of segmentation and noise/pedicel removal is illustrated in Fig. 4.

As it can be checked, I_{Bin2} is an accurate segmentation of olives from the background. However, olives in touch appear fused building enlarged connected components (sets of neighbor pixels). The aim of the procedure described in section III-B will be to separate olives fused in I_{Bin2}, so as to every connected component corresponds to a single olive. With this goal, preprocessing finishes by computing the

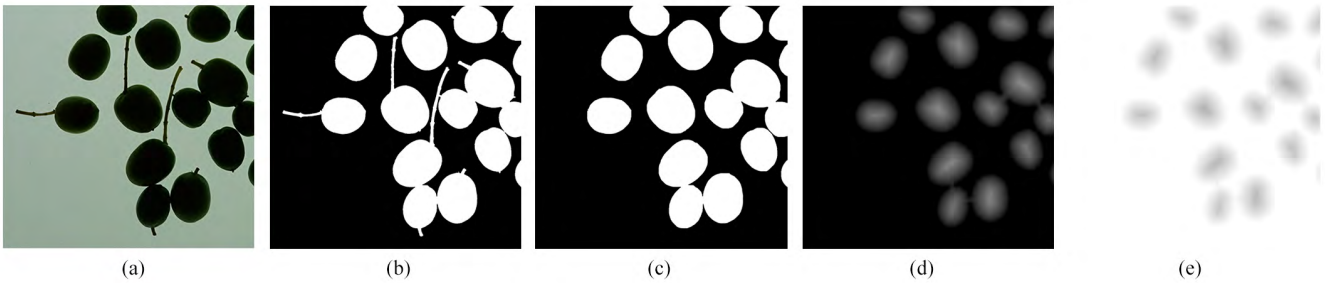

FIGURE 4. Illustration of the image preprocessing: (a) original sub-image; (b) binary sub-image; (c) binary sub-image after noise and pedicel removal; (d) distance transform of image (c); (e) complement of the image (d).

distance transform DT on I_{Bin2}, which calculates, for every pixel, its Euclidean distance to its nearest background pixel:

$$I_{DT} = DT\left(I_{Bin2}\right), \tag{4}$$

where, DT is mathematically formulated as:

$$[DT(I_{Bin2})](x,y) = min\left\{\sqrt{(x-x')^2+(y-y')^2} \mid I_{Bin2}\left(x',y'\right)=0\right\} \tag{5}$$

This information will be key for olive separation in I_{Bin2}. Indeed, I_{DT} is a meaningful and simplified image in which the mass center of all olives, originally in touch or not, constitute a regional maximum for being the local farthest point to the background (see Fig. 4-(d)). Note that a generic regional maximum M of an image can be defined as a set of neighbor pixels with a given grey-level value v, such that every pixel in the neighborhood of M has a value strictly lower than v. The entire preprocessing is illustrated in Fig. 4.

B. INDIVIDUAL OLIVE SEGMENTATION

The goal at this stage is the accurate application of the Watershed transform to individually segment olives in image I_{Bin2}. Conceptually, the Watershed approximates an image as a topographic surface, where grey-level values represent altitudes, being the darker regions taken as catchment basins. Then, the surface is flooded, and the basins are divided by water convergence lines, whose path is influenced by the deepness, size and shape of basins. Formally, the definition and implementation of the Watershed transform is not obvious and has produced a great amount of specific literature over the years, which is encouraged to be consulted for deeper study [28], [29].

According to the given explanation, if the complement image of I_{DT}, $\overline{I_{DT}} = 255 - I_{DT}$ (see Fig. 4-(e)), is seen as a topographic surface, olives constitute catchment basins. Additionally, these basins are ideally divided by draining lines traced according to the influence produced by the characteristics of every basin with respect to its surroundings. However, the direct application of the Watershed to $\overline{I_{DT}}$ would produce oversegmentation with high probability, as it is well-known to be very sensitive to local irregularities [29]. To overcome this difficulty, a marker-controlled Watershed segmentation is proposed [30]. A marker is a connected component belonging to the image to be segmented. Thus, internal markers, those inside olives, and external markers, belonging to the background, are found. Then, they are used to limit the regions allowable by the watershed to those of olives, and to accordingly modify the gradient of the image.

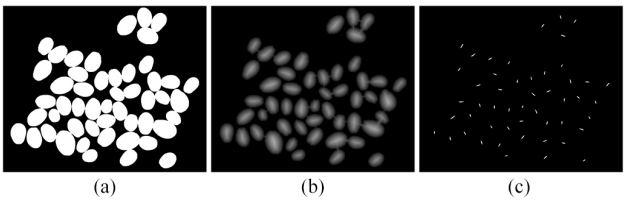

FIGURE 5. (a) starting binary image, I_{Bin2}; (b) image resulting after applying the distance transform on (a), I_{DT}; (c) extended regional maxima of (b), $I_{RMaxBin}$.

As a first step to obtain the set of internal markers, the regional maxima located at the olive centres in image I_{DT} are extracted by applying the *h-maxima* transform [23, pp. 201-204]. This transform firstly removes irrelevant regional maxima from the image, which will be those with a height lower or equal than h. Mathematically:

$$I_{HMax} = R^{\delta}_{I_{DT}}\left(I_{DT} - h\right), \tag{6}$$

where, generically, $R^{\delta}_{I_{Mask}}(I_{Marker})$ is the morphological reconstruction by dilation of I_{Mask} from marker I_{Marker}, using a unitary structuring element [31]. Respecting parameter h, a value of 5 was enough to retain only significative maxima (the choice of this parameter value was proven to have a wide range of optimum values in this particular case). Next, the surviving relevant regional maxima in image I_{HMax} are extracted by computing:

$$I_{RMax} = I_{HMax} - R^{\delta}_{I_{HMax}}(I_{HMax} - 1), \tag{7}$$

and thresholding the resulting image:

$$I_{RMaxBin}(x,y) = \begin{cases} 255 & if\ I_{RMax}(x,y) > 0 \\ 0 & in\ any\ other\ case, \end{cases} \tag{8}$$

The result of operations (6)-(8) can be consulted in Fig. 5.

At this point, the exact number N of fruits present in the image, originally in touch or not, is obtained by counting

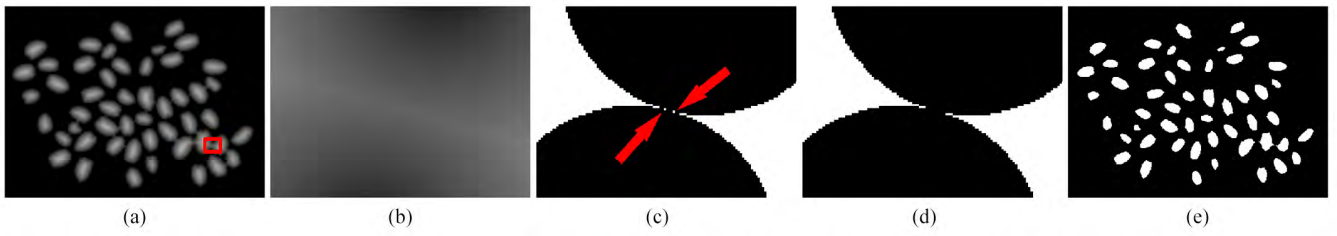

FIGURE 6. Generation of the image of internal markers, I_{IntMk}: (a) image of the distance function; (b) close-up of the red-squared zone in image (a); (c) binarization of (b) with a threshold Th_{Min} value of 65; (d) removal of the artificial connected components thanks to operation (9); (e) Image I_{IntMk}, where each connected component represents an internal marker for the application of the watershed transform.

the number of connected components present in $I_{RMaxBin}$. Next, this information is exploited to finally decide the set of internal markers, by building a binary image in which all olive fruits are disconnected, but in such a way that they keep their spatial relationship/influence; note that this constraint preserves the original major draining lines. To do so, the objective is finding the minimum threshold value, Th_{Min}, producing a binarization of the distance transform image, I_{DT}, exactly containing N connected components corresponding to the olives disaggregated. Indeed, assuming that the image contains olives in touch, the lower the threshold value is, the lower the number of connected components contains the binary image as they tend to fuse building aggregations. Contrary, as the threshold value increases, the olives tend to disconnect, and the number of connected components converge to N. However, there are two situations to consider in the solution for finding Th_{Min}: 1) smaller olives may disappear when binarizing image I_{DT} from a certain threshold value, depending on the size of the larger ones and the size of aggregations; 2) tiny artificial connected components may appear when binarizing I_{DT} as a consequence of the discrete and quantized nature of the image (check Fig. 6-(a) to (c)).

Therefore, the mathematical solution to the described problem, which provides the set of internal markers, can be formulated as follows:

$$I_{IntMk} = R^{\delta}_{I_{Cand}}\left(I_{RMaxBin}\right), \tag{9}$$

where I_{IntMk} contains N connected components corresponding to the individual olives, being

$$I_{Cand} = max\{I_{ThMin}, I_{RMaxBin}\} \tag{10}$$

Indeed, the morphological reconstruction planned in (9) discards the previously pointed out artificial connected components probably present in I_{Cand} (check Fig. 6-(c)-(e)). Additionally, (10) recovers in I_{Cand} the smaller connected components that may have disappeared when calculating I_{ThMin}. Thus, I_{ThMin} is the binarization of the distance transform image I_{DT}:

$$I_{ThMin}(x,y) = \begin{cases} 255 & if\ I_{DT}(x,y) > ThMin \\ 0 & in\ any\ other\ case \end{cases} \tag{11}$$

when $ThMin$ takes the minimum threshold value for which I_{IntMk} contains N connected components (given by the generic function CC),

$$Th_{Min} = min\{t \mid CC\left(I_{IntMk}\right) = N, t = 0, \ldots, 254\} \tag{12}$$

Consequently, in order to computationally determine Th_{Min}, an incremental iterative binarization over every possible threshold value starting from 1 is performed. Thus, by binarizing the distance-transform image I_{DT} at every value, Th_{Min} is decided when the resulting image contains an equal number of connected components, N, than the regional maxima image, I_{IntMk}.

Next image $I_{DT_{IntMk}}$ resulting from the application of the distance transform (5) to I_{IntMk} is calculated (Fig 7-(a)). Then, the set of external markers is obtained by applying the Watershed transform to the complement of $I_{DT_{IntMk}}$, $\overline{I_{DT_{IntMk}}}$, as follows:

$$I_{ExtMk}(x,y) = \begin{cases} 0 & if\ [WS(\overline{I_{DT_{IntMk}}})](x,y) = 0 \\ 1 & in\ any\ other\ case \end{cases}, \tag{13}$$

where WS stands for Watershed transform. The steps to obtain this marker-image are visually represented in Fig. 7. Note that the external markers are the dark lines illustrated in Fig. 7–(c).

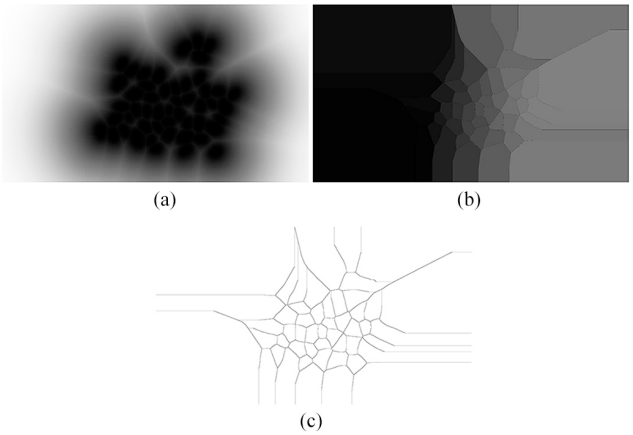

FIGURE 7. Computation of the set of external markers $I_{ExtMark}$: (a) $\overline{I_{DT_{IntMk}}}$, which results from inverting the image resulting from the application of the distance transform to the image of internal markers $I_{IntMark}$; (b) image $WS(\overline{I_{DT_{IntMk}}})$, resulting from the application of the watershed transform to $\overline{I_{DT_{IntMk}}}$ (a); (c) image of external markers (dark lines), $I_{ExtMark}$, resulting from binarizing $WS(\overline{I_{DT_{IntMk}}})$ (b).

At this point, it should be noted that the set of lines integrating the external markers offer a partial solution to the separation problem, but it often provokes oversegmentation. Thus, the external markers are used to force the occurrence of regional minima (operation known as minima imposition [23, pp. 172-173]) in the complement distance transform image $\overline{I_{DT}}$, as:

$$I_{MinImp} = R^{\varepsilon}_{min\{\overline{I_{DT}}, I_{ExtMark}\}}(I_{ExtMark}) \tag{14}$$

where, generically, $R^{\varepsilon}_{I_{Mask}}(I_{Marker})$ is the morphological reconstruction by erosion of I_{Mask} from marker I_{Marker}, using a unitary structuring element [31]. After this minima imposition, the Watershed transform is applied to I_{MinImp}, thus providing the definitive set of ridge lines used to eventually separate the olives in I_{Bin2} as:

$$I_{Final} = min\{I_{Bin2}, I_{Lines}\}, \tag{15}$$

where

$$I_{Lines}(x, y) = \begin{cases} 0 & if\ [WS\left(\overline{I_{MinImp}}\right)](x, y)] = 0 \\ 1 & in\ any\ other\ case \end{cases}, \tag{16}$$

The definitive outcome at this stage, I_{Final}, is shown in Fig. 8.

C. IMAGE POSTPROCESSING

Once object separation is finished, tiny artificial connected components may have been generated as a consequence of the application of the Watershed transform. These exceptional oversegmentation occurrences are removed by computing a morphological opening, followed by a reconstruction of the resulting image to restore the exact size and shape of the surviving connected components. Mathematically:

$$I_{Olives} = R^{\delta}_{I_{Final}}(I_{Aux}) \tag{17}$$

$$I_{Aux} = \gamma_{\beta}(I_{Final}) \tag{18}$$

β represents the disk-shaped structuring element used in the opening operation. Its radius length is adaptatively computed per variety as follows:

$$\beta = \overline{r^v} - 5 \times \sigma_r^v - 1, \tag{19}$$

where $\overline{r^v}$ and σ_r^v are, respectively, the mean and the sample standard deviation values defining the statistical distribution of observations of the minor radius length of the connected components present in I_{Final}. The distributions were studied for each variety v by analyzing all the images with the methodology described in sections III-A and III-B, and using the procedure detailed in section III-D to calculate the radius length values. Hence, the distribution of olive sizes per variety is assumed to be Gaussian, and only extremely non-representative examples, those out of the average minus five times the standard deviation, are discarded for being too tiny to be meaningful.

Finally, postprocessing ends with removing from I_{Olives} those olives not completely contained in the image. To do so, those connected components reaching the border in I_{Olives} are discarded by performing:

$$I_{OlivesDef} = I_{Olives} - R^{\delta}_{I_{Olives}}(I_{BorderSeeds}), \tag{20}$$

where $I_{BorderSeeds}$ contains seeds for each olive connected to the image border

$$I_{BorderSeeds} = min\{I_{Olives}, I_{Border}\}, \tag{21}$$

and I_{Border} is a border image

$$I_{Border}(x, y) = \begin{cases} 255 & if\ \ (x, y)\ is\ a\ border\ pixels \\ 0 & in\ any\ other\ case \end{cases}\Big\} \tag{22}$$

This subprocess is illustrated in Fig. 9 by treating a subimage instead of a full capture. This, in order to make easier its visualization.

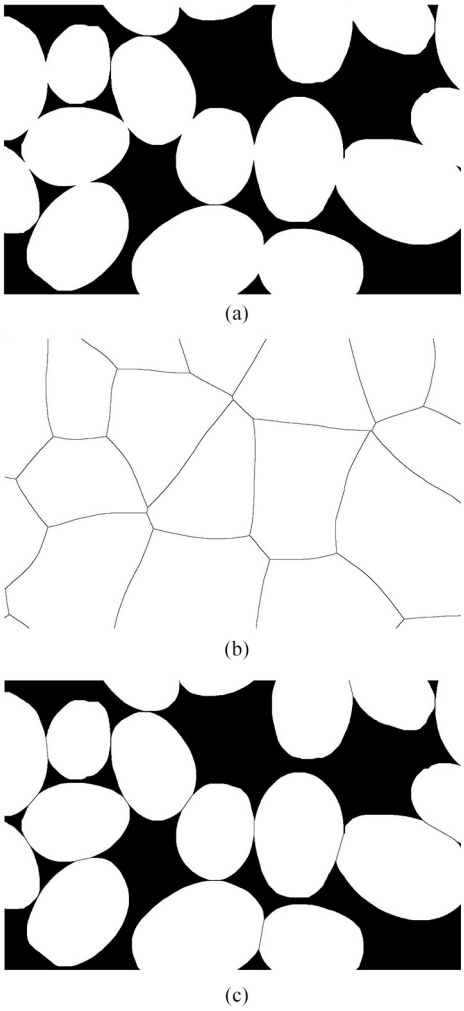

FIGURE 8. Illustration of final olive separation: (a) binary image I_{Bin2} with olive aggregations to be separated; (b) ridge lines obtained by marked-controlled watershed segmentation; (c) binary image, after olive-fruit separation, which is calculated as the minimum value of (a) and (b) for every pixel.

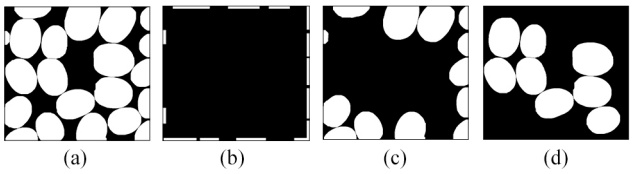

FIGURE 9. Illustration of the removal of the olives that are not completely contained in the image: (a) binary image after individual olive segmentation; (b) seeds corresponding to each of the olives connected to the border; (c) components corresponding to the olives connected to the border; (d) result after components in (c) are removed from (a).

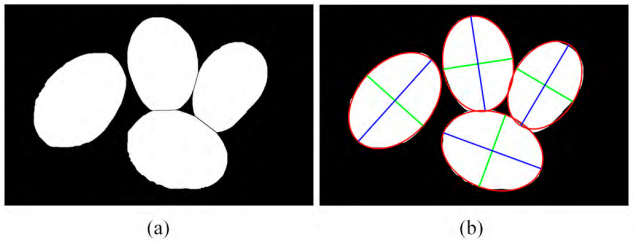

FIGURE 10. Representation of the ellipses, and their corresponding axes, computed for characterizing olive-fruit size.

It should be noted that in Fig. 9-(b), seeds have been expanded and exaggerated for the purpose of facilitating its visual representation.

D. OLIVE SIZE AND MASS CHARACTERISATION

The image analysis methodology presented individually segmented olive-fruits following the principles specified in section III-B. At this point, the objective is the formulation of descriptive features, measurable in the segmented images, to approach the major and minor axis length, and mass, of every individual olive. Finally, these features are exploited to build estimation models.

First, the major and minor axis length of an olive are proposed to be characterized by the length in pixels of the two axes of the ellipse having the same normalized second central moment [32] than its connected component:

$$MajAx\left(CC_i\right) = \max\left(E_{D_1}\left(CC_i\right), E_{D_2}\left(CC_i\right)\right), \quad CC_i \subseteq I_{Olives}, \tag{23}$$

$$MinAx\left(CC_i\right) = \min\left(E_{D_1}(CC_i), E_{D_2}(CC_i)\right), \quad CC_i \subseteq I_{Olives}, \tag{24}$$

E_{D_1} and E_{D_2} denotes the diameters, D_1 and D_2, of the two axes of ellipse E fulfilling the previous definition for connected component CC_i of image I_{Olives}. This approach is illustrated in Fig. 10.

Second, for characterizing mass of an olive, the area in pixels of its corresponding connected component is considered. The first approach to this proposal is to assume the extent to which each pixel equally contributes to the mass characterization, independently of its position within the connected component. Mathematically:

$$Area\left(CC_i\right) = \#CC_i, \quad CC_i \subseteq I_{Olives}, \tag{25}$$

where # stands for the cardinal operation.

Additionally, a set of alternative approaches, based on pixel weighing, are proposed as well. It should be noted that a connected component is, in fact, a 2D projection of an olive, which actually has an ellipsoidal three-dimensional body. In order to introduce this notion of three-dimensionality, it seems reasonable to consider that the contribution of a given pixel, when approximating the mass of the fruit, must be greater the closer this pixel is to the mass center of the corresponding connected component. This argument suggests weighing the contribution of every pixel according to its relative location within the connected component which it belongs to.

Therefore, it is proposed a pixel-weighing scheme by means of the application of the distance transform in conjunction with a set of functions, aimed to express the pursued three-dimensionality.

Hence, the area of a connected component CC_i contained in image I_{Olives}, is calculated using a generic weighing function w, as:

$$Area_w(CC_i) = \sum\nolimits_{(x,y)\in CC_i} w\left(\left[NDT_v\left(I_{Olives}\right)\right](x,y)\right), \quad CC_i \subseteq I_{Olives} \in v \tag{26}$$

NDT_v refers to the distance transform function (4), normalized by the maximum olive-to-background pixel distance measured throughout the whole set of processed images, for the corresponding olive variety v (27), as shown at the bottom of this page.

The purpose of the weighing function is to modulate the initial weights, provided by the application of the distance transform, according to the ellipsoidal shape of the fruits. To this end, logarithm- and root-based functions are selected and studied, since the draw similar shapes to that observable in a cross-sectional view of an olive.

Therefore, the proposed weighing functions w, and the labels they will be referred with from now on, are defined as:

- Natural logarithm (NLog):

$$w\left(p\right) = ln(1 + (e-1) \times p) \tag{28}$$

- Logarithm to base n (Log_n):

$$w\left(p\right) = \log_n\left(1 + (n-1) \times p\right), \quad n = 2, 3, 5, 10 \tag{29}$$

- Square root (Root_n):

$$w\left(p\right) = \sqrt[n]{p}, \quad n = 2, 3, 5, 7, 10 \tag{30}$$

The representation as an image of the application of the different weighing functions is illustrated in Fig. 11, where the weigh assigned to each pixel is represented as a grey-level value. All these alternatives will later be evaluated and compared.

E. OLIVE SIZE AND MASS MODEL TRAINING

For training estimation models for olive minor and major axis length, and mass, a set of 100 olive-fruits was built per variety

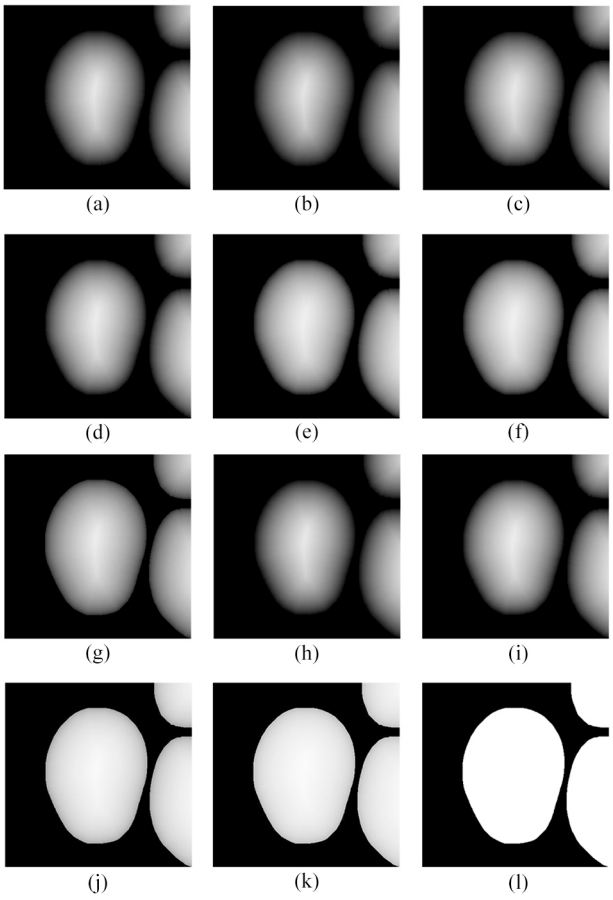

FIGURE 11. Pixel-weighing representation for each of the mass models considered: (a) NLog; (b) Log_2; (c) Log_3; (d) Log_5; (e) Log_7; (f) Log_{10}; (g) $Root_2$; (h) $Root_3$; (i) $Root_5$; (j) $Root_7$; (k) $Root_{10}$; (l) representation of equally-weighed pixels.

(900 in total), thus keeping disjoint sets of 300 individuals per variety for external validation (2,700 in total). The sets for training were made up with samples representing the particular observed variability for each olive variety in terms of size and mass. On the other hand, the images containing the training olive samples were analyzed, and the features described above were calculated for all of them. Then, a linear regression analysis was performed per variety on the training instances. It allowed to model the relationship between the magnitude of the features given by image analysis and the corresponding objective data previously registered in laboratory. This training scheme produced three estimation models per variety, one per feature, which will be referred as variety-dependent estimation models hereafter. In addition, the linear regression analysis was replicated by considering the nine different training sets as a whole. It made possible to generate and assess the behavior of a unique set of three estimation models applicable to all varieties. These models will be called variety-independent estimation models from here on.

F. APPROACH FOR THE METHODOLOGY'S PERFORMANCE EVALUATION

The performance of the proposed methodology was assessed following a double approach.

First, the ability of the image analysis algorithm to individually segment olives was studied. For this purpose, the 72 regular images (8 per variety), containing 50 olives each, were processed with the algorithm, and the number of individual olives found was evaluated. Additionally, the algorithm was also challenged under this criterion by analyzing the set of 45 stress images (5 per variety).

Second, the behavior of the whole methodology, comprising the image analysis algorithm and the different estimation models, was assessed. For each of the three modelled features, olive major and minor axis length, and mass, estimations given by the methodology were confronted to the reference values obtained in laboratory using the following proposed metrics:

- Root-Mean-Square Error:

$$RMSE = \sqrt{\frac{\sum_{i=1}^{n} (\hat{y}_i - y_i)^2}{n}} \tag{31}$$

- Relative Root-Mean-Square Error (expressed as percentage):

$$SE = \frac{RMSE}{\frac{\sum_{i=1}^{n} y_i}{n}} \times 100 \tag{32}$$

- Relative Mean Error (expressed as percentage):

$$|E| = \frac{\left|\sum_{i=1}^{n} (\hat{y}_i - y_i)\right|}{\sum_{i=1}^{n} y_i} \times 100 \tag{33}$$

where, for the *i-th* fruit of a set of n elements, $\hat{y}_i$ refers to the predicted value and y_i stands for its corresponding reference measure. Additionally, one-way analysis of variance was also conducted on the estimation results of the different developed models for the nine varieties. Mean comparison was attempted, performing the Tukey's test [33] at $p < 0.05$, on the population of individual relative errors, e_i, defined as the ratio between the estimated and the actual value considered:

$$e_i = \frac{\hat{y}_i}{y_i} \tag{34}$$

At this point, it is important to recall that the minor and major axis length of 100 olives per variety (900 in total) were measured by three different observers. For these samples and

$$[NDT_v(I_{Olives})](x, y) = \frac{[DT\,(I_{Olives})]\,(x, y)}{max\left\{\sqrt{\left(x' - x''\right)^2 + \left(y' - y''\right)^2} \,|\, I'_{Olives}\left(x', y'\right) = 255 \wedge I''_{Olives}\left(x'', y''\right) = 0\right\}}, \tag{27}$$

TABLE 2. Fruit-detection accuracy tested on stress images.

Variety	Stress Images					
	stress_image_0 (detected/actual fruits)	stress_image_1 (detected/actual fruits)	stress_image_2 (detected/actual fruits)	stress_image_3 (detected/actual fruits)	stress_image_4 (detected/actual fruits)	Overall (detected/actual fruits success rate)
967	103/103	165/165	187/187	254/254	311/311	1020/1020
1030	138/138	182/182	210/210	246/246	323/323	1099/1099
Arbequina	158/158	194/194	221/221	251/249	304/303	1128/1125
Arbosana	111/111	137/137	190/190	250/250	355/355	1043/1043
Changlot	66/66	91/91	117/117	156/156	237/237	667/667
Lechín	71/71	112/112	153/153	211/211	258/257[b]	805/804
Ocal	95/95	100/100	113/113	117/117	141/141	566/566
Picual	164/164	195/195	207/207[a, b]	233/233	256/256	1055/1055
Verdial	64/64	91/91	112/112	140/140	220/220	627/627
	-	-	-	-	-	8110/8106

[a] Denotes underestimation occurrence.
[b] Denotes overestimation occurrence.

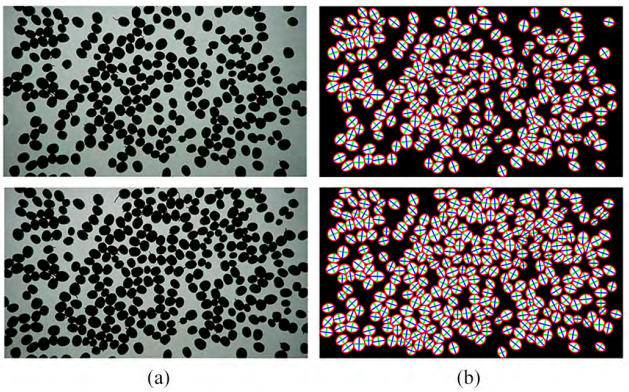

FIGURE 12. Examples of stress-images captured for variety 967 (a), and the corresponding results after processing/analysis algorithm is applied (b).

features, the average of the three independent observations was used as reference measure y_i for the application of the metrics above. Notwithstanding, the motivation for performing this multiple evaluation for a subset of olives, was to investigate the degree of uncertainty induced by the observer when measuring the olive axis with a digital caliper. With this purpose, the *SME* metric was defined as:

$$SME = \frac{\sum_{i=1}^{n} ISME_i}{n} \times 100, \tag{35}$$

where

$$ISME_i = \frac{max\{|y_{i,j} - \overline{y_i}|\}}{\overline{y_i}} \tag{36}$$

Indeed, for every fruit i involved in the study, an error $ISME_i$ was defined as the absolute maximum deviation of the three observations $y_{i,j}, j = 1, \ldots, 3$, with respect to the mean value of the observations $\overline{y_i}$.

IV. RESULTS AND DISCUSSIONS

A. RESULTS OF THE IMAGE ANALYSIS ALGORITHM

The image analysis algorithm showed 100% of accuracy when individually segmenting olives in the case of the 72 regular images, as it exactly segmented 50 olives in all of them (3,600 in total), independently from the olive variety considered. With respect to the 45 stress images, they represented a very more complex and challenging scenario for the algorithm, as they contained numerous olives chaotically positioned, with multiple border cuts and olive touching occurrences to deal with.

Fig. 12 illustrates a set of stress-images and the graphical representation of the results of their analysis.

As it can be observed, the algorithm showed great ability to individually segment olives and to discard those cut by the image borders. This visual impression was corroborated by the numerical analysis of the results given in Table 2. This table compiles the results regarding fruit-detection

TABLE 3. External validation results calculated considering all varieties as a whole (N = 2,700).

Feature	Model type	RMSE	SE (%)	|E| (%)
Major axis	Variety-dependent	0.4956 (mm)	2.67	0.44
	Variety-independent	0.5714 (mm)	3.07	1.14
Minor axis	Variety-dependent	0.3543 (mm)	2.47	0.34
	Variety-independent	0.3711 (mm)	2.57	0.60
Mass:	Variety-dependent	0.1192 (g)	5.20	0.55
Area	Variety-independent	0.2106 (g)	9.89	6.46
Mass:	Variety-dependent	0.1134 (g)	4.84	0.51
$\boldsymbol{Area_{NLog}}$	Variety-independent	0.2806 (g)	13.53	9.05
Mass:	Variety-dependent	0.1135 (g)	4.84	0.50
$\boldsymbol{Area_{Log_2}}$	Variety-independent	0.2878 (g)	13.87	9.39
Mass:	**Variety-dependent**	**0.1132 (g)**	**4.84**	**0.49**
$\boldsymbol{Area_{Log_3}}$	Variety-independent	0.2783 (g)	13.42	8.95
Mass:	Variety-dependent	0.1132 (g)	4.85	0.49
$\boldsymbol{Area_{Log_5}}$	Variety-independent	0.2675 (g)	12.89	8.43
Mass:	Variety-dependent	0.1139 (g)	4.88	0.54
$\boldsymbol{Area_{Log_{10}}}$	Variety-independent	0.2550 (g)	12.27	7.76
Mass:	Variety-dependent	0.1141 (g)	4.89	0.56
$\boldsymbol{Area_{Root_2}}$	Variety-independent	0.2488 (g)	11.94	7.38
Mass:	Variety-dependent	0.1147 (g)	4.95	0.50
$\boldsymbol{Area_{Root_3}}$	Variety-independent	0.2329 (g)	11.12	6.47
Mass:	Variety-dependent	0.1161 (g)	5.03	0.51
$\boldsymbol{Area_{Root_5}}$	Variety-independent	0.2222 (g)	10.55	6.40
Mass:	Variety-dependent	0.1170 (g)	5.08	0.54
$\boldsymbol{Area_{Root_7}}$	Variety-independent	0.2183 (g)	10.34	6.36
Mass:	Variety-dependent	0.1176 (g)	5.11	0.54
$\boldsymbol{Area_{Root_{10}}}$	Variety-independent	0.2157 (g)	10.19	6.38

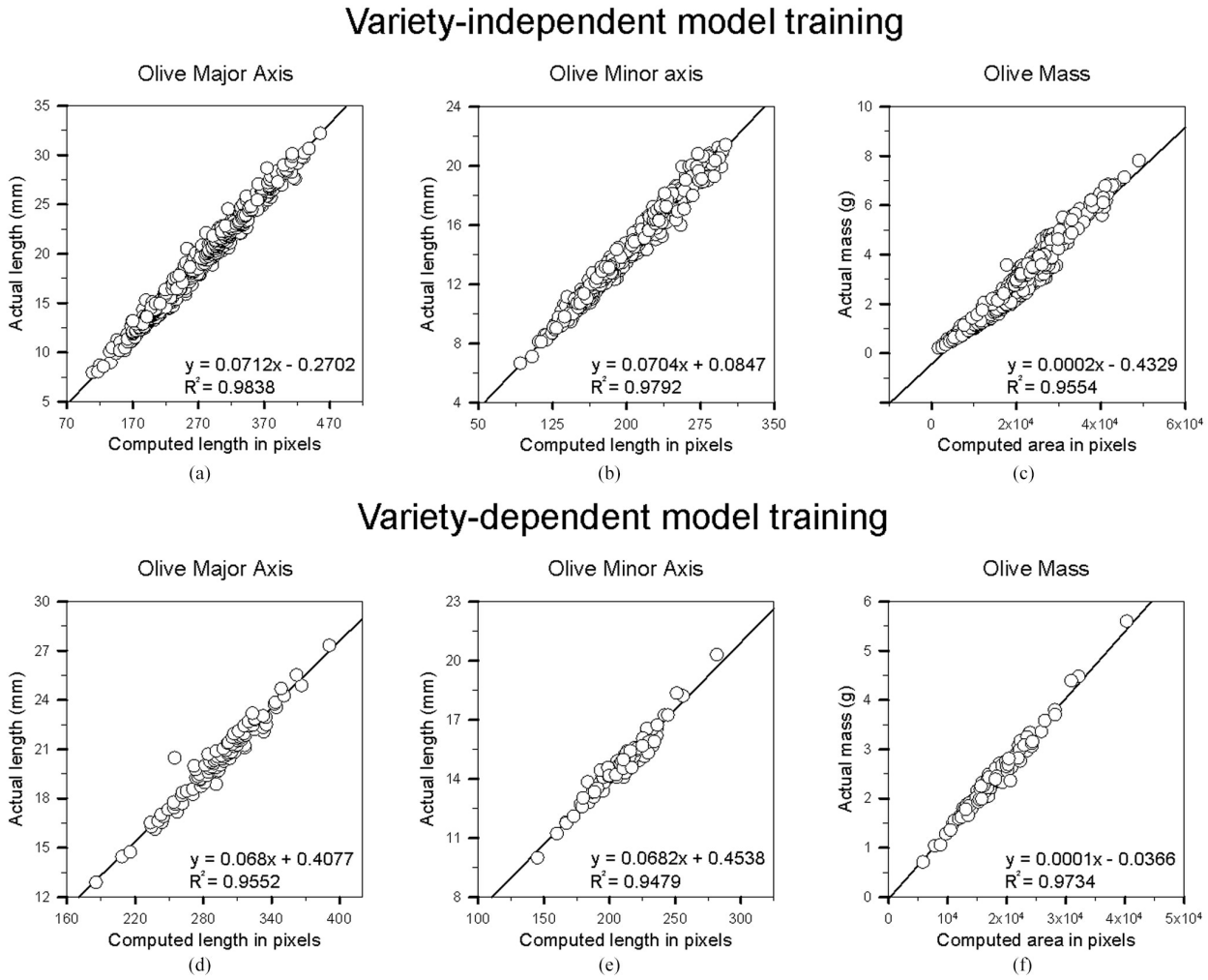

FIGURE 13. Representation of the regression analysis performed to compute the different variety-independent and -dependent models: (a) major-axis-length variety-independent model; (b) minor-axis-length variety-independent model; (c) $Area_{Log_3}$ mass variety-independent model; (d) major-axis-length model for changlot real variety; (e) minor-axis-length model for changlot real variety; (f) $Area_{Log_3}$ mass model for changlot real variety.

accuracy, by showing the ratio between the olives detected and the actual number of fruits which appear in the corresponding stress images.

An outstanding number of 8,106 olive instances were present in the 45 stress images. The algorithm individually segmented 8,110. This slight deviation responds to the overestimation of 5 olives in 4 different stress images, all of them related to not correctly removing olives cut by the image border. Additionally, there was only one case of underestimation in which a pair of fruits, touching each other, were not properly separated; it occurred in image *stress_image_2* of the Picual variety. Thus, if 6 segmentation errors are counted over 8106 cases, it can be concluded that the accuracy of the algorithm measured on the stress images was 99.92%.

B. RESULTS OF THE WHOLE METHODOLOGY FOR ESTIMATING OLIVE-FRUITS MASS AND SIZE

A set of 27 variety-dependent models (9 varieties × 3 features), and a set of 3 variety-independent models (1 per feature for all varieties), were obtained by linearly correlating the features obtained by image analysis to the actual reference measures. Overall, those mass estimation models trained featuring olive mass with the weighing function $Area_{Log_3}$ (eq. (23), $n = 3$), provided better performance at external validation than most of the other approaches. Table 3 summarizes the results of this comparison computed on the external validation sets presenting, per model tentative, the mean value of the previously defined error metrics calculated for each olive variety. Consequently, the discussion and the results reviewed hereafter regarding mass estimation are referred to this choice.

Fig. 13 illustrates the correlation results registered when training the three independent models and, as an example, the three dependent models for Changlot Real variety. As it can be observed, there was a significant positive correlation, exhibiting a minimal degree of dispersion in all the cases. This fact, extendable to the rest of the models computed, highlights a strong statistical relationship between the

TABLE 4. Training and external validation results for each of the estimation models proposed and varieties studied. N = 900 for model training (100 per variety), and N = 2,700 for validation (300 per variety).

			TRAINING		EXTERNAL VALIDATION		
Variety	Feature	Model type	R^2	Regression equation	*RMSE*	*SE* (%)	|*E*| (%)
967	Major axis	Variety-dependent	0.9407	y=0.06427x+0.95664	0.3946	2.64	0.68
		Variety-independent	0.9838	y=0.07124x-0.27022	0.4242	2.84	1.17
	Minor axis	Variety-dependent	0.9544	y=0.06724x+0.47133	0.3708	2.95	1.04
		Variety-independent	0.9792	y=0.07037x+0.08466	0.3474	2.76	0.32
	Mass: $Area_{Log_3}$	Variety-dependent	0.9756	y=0.00012x-0.03778	0.0715	5.07	0.63
		Variety-independent	0.9554	y=0.00016x-0.43286	0.1652	11.71	5.16
1030	Major axis	Variety-dependent	0.9439	y=0.06515x+1.01841	0.3478	2.42	0.53
		Variety-independent	0.9838	y=0.07124x-0.27022	0.3862	2.69	0.86
	Minor axis	Variety-dependent	0.9652	y=0.06913x+0.33592	0.2528	2.16	0.02
		Variety-independent	0.9792	y=0.07037x+0.08466	0.2584	2.21	0.41
	Mass: $Area_{Log_3}$	Variety-dependent	0.9836	y= 0.00014x-0.03032	0.0456	3.88	0.15
		Variety-independent	0.9554	y=0.00016x-0.43286	0.1976	16.79	15.19
Arbequina	Major axis	Variety-dependent	0.9772	y= 0.06448x+0.9561	0.5037	3.42	0.58
		Variety-independent	0.9838	y=0.07124x-0.27022	0.5710	3.88	0.83
	Minor axis	Variety-dependent	0.9747	y= 0.06771x+0.51259	0.2889	2.17	0.17
		Variety-independent	0.9792	y=0.07037x+0.08466	0.3052	2.29	0.40
	Mass: $Area_{Log_3}$	Variety-dependent	0.9886	y= 0.00013x+0.02085	0.1106	7.11	0.60
		Variety-independent	0.9554	y=0.00016x-0.43286	0.2109	13.57	7.65
Arbosana	Major axis	Variety-dependent	0.9645	y= 0.06933x+0.04436	0.3154	2.22	0.11
		Variety-independent	0.9838	y=0.07124x-0.27022	0.3321	2.34	0.41
	Minor axis	Variety-dependent	0.9471	y=0.06897x+0.29699	0.2260	2.01	0.18
		Variety-independent	0.9792	y=0.07037x+0.08466	0.2336	2.08	0.28
	Mass: $Area_{Log_3}$	Variety-dependent	0.9816	y=0.00011x+0.00384	0.0435	4.02	0.34
		Variety-independent	0.9554	y=0.00016x-0.43286	0.1844	17.01	6.87
Changlot Real	Major axis	Variety-dependent	0.9552	y=0.06801x+0.4077	0.5938	2.89	0.78
		Variety-independent	0.9838	y=0.07124x-0.27022	0.5970	2.91	0.54
	Minor axis	Variety-dependent	0.9479	y=0.06824x+0.45384	0.3035	2.06	0.45
		Variety-independent	0.9792	y=0.07037x+0.08466	0.2988	2.03	0.06
	Mass: $Area_{Log_3}$	Variety-dependent	0.9734	y=0.00014x-0.03664	0.1056	4.25	1.16
		Variety-independent	0.9554	y=0.00016x-0.43286	0.1601	6.44	0.70
Lechín de Sevilla	Major axis	Variety-dependent	0.9451	y=0.0734x-0.76493	0.5755	2.76	0.24
		Variety-independent	0.9838	y=0.07124x-0.27022	0.5913	2.84	0.92
	Minor axis	Variety-dependent	0.8791	y=0.06498x+1.13778	0.3418	2.30	0.27
		Variety-independent	0.9792	y=0.07037x+0.08466	0.3755	2.53	0.86
	Mass: $Area_{Log_3}$	Variety-dependent	0.9673	y=0.00012x+0.00431	0.1059	4.15	0.28
		Variety-independent	0.9554	y=0.00016x-0.43286	0.4007	15.71	12.46
Ocal	Major axis	Variety-dependent	0.9282	y=0.06567x+1.93467	0.7471	2.89	0.64
		Variety-independent	0.9838	y=0.07124x-0.27022	0.8365	3.24	1.37
	Minor axis	Variety-dependent	0.8463	y=0.06721x+1.0975	0.5275	2.79	0.38
		Variety-independent	0.9792	y=0.07037x+0.08466	0.5980	3.16	1.32
	Mass: $Area_{Log_3}$	Variety-dependent	0.9596	y=0.00015x+0.22991	0.2986	5.91	0.85
		Variety-independent	0.9554	y=0.00016x-0.43286	0.5747	11.37	9.68
Picual	Major axis	Variety-dependent	0.9486	y=0.0692x+0.87548	0.4525	2.32	0.20
		Variety-independent	0.9838	y=0.07124x-0.27022	0.7827	4.01	3.25
	Minor axis	Variety-dependent	0.9406	y=0.06963x+0.37024	0.2990	2.32	0.14
		Variety-independent	0.9792	y=0.07037x+0.08466	0.3276	2.55	1.03
	Mass: $Area_{Log_3}$	Variety-dependent	0.9773	y=0.00012x-0.07138	0.0749	4.17	0.27
		Variety-independent	0.9554	y=0.00016x-0.43286	0.3767	20.97	18.42
Verdial de Huevar	Major axis	Variety-dependent	0.9492	y=0.06607x+1.14255	0.5299	2.50	0.20
		Variety-independent	0.9838	y=0.07124x-0.27022	0.6221	2.94	0.94
	Minor axis	Variety-dependent	0.8506	y= 0.06252x+1.98224	0.5783	3.47	0.40
		Variety-independent	0.9792	y=0.07037x+0.08466	0.5956	3.58	0.74
	Mass: $Area_{Log_3}$	Variety-dependent	0.9658	y= 0.00015x+0.00958	0.1622	4.97	0.11
		Variety-independent	0.9554	y=0.00016x-0.43286	0.2348	7.20	4.44

estimations and actual values, which reinforce the viability of using simple-linear-regression-based modelling in order to individually estimate the mass and size of olive-fruits.

Table 4 details training and external validation results for all the model variants and olive varieties. With regard to training, outstandingly high values were registered for the coefficient of determination, R^2, in all cases. Indeed, the coefficient value was below 0.9 only in three cases, reaching 0.8463 in the worst case. Furthermore, training was generally so consistent and comparable for both the variety-dependent and the variety-independent approaches, that no conclusions could be taken at this stage. However, when applying the

TABLE 5. Results of one-way analysis of variance performed on the estimations produced by the variety-dependent and -independent models for each variety. The analyzed populations are the individual relative errors, calculated by using (34), produced by the different models on the external validation sets of each variety (N = 2,700, 300 per variety). The mean $\overline{e_i}$ and standard deviation σ_{e_i} of each population is given. dissimilar letters indicate different statistical means according to the analysis of variance using the tukey's test at $p < 0.05$.

Variety	Variety-dependent models			Variety-independent models		
	Major axis $(\overline{e_i}, \sigma_{e_i})$	Minor axis $(\overline{e_i}, \sigma_{e_i})$	Mass: $Area_{Log_3}$ $(\overline{e_i}, \sigma_{e_i})$	Major axis $(\overline{e_i}, \sigma_{e_i})$	Minor axis $(\overline{e_i}, \sigma_{e_i})$	Mass: $Area_{Log_3}$ $(\overline{e_i}, \sigma_{e_i})$
967	(0.9944,0.0265) [a]	(0.9907,0.0276) [a]	(0.9964,0.0488) [ab]	(1.0117,0.0268) [d]	(1.0039,0.0279) [de]	(1.0225,0.1314) [d]
1030	(0.9952,0.0243) [a]	(1.0003,0.0218) [bc]	(1.0020,0.0468) [b]	(0.9909,0.0264) [b]	(0.9961,0.0219) [bc]	(0.8148,0.1503) [a]
Arbequina	(0.9950,0.0339) [a]	(0.9985,0.0223) [bc]	(0.9974,0.0758) [ab]	(1.0071,0.0377) [cd]	(1.0037,0.0232) [de]	(0.8770,0.1725) [b]
Arbosana	(0.9989,0.0234) [ab]	(1.0018,0.0204) [bc]	(0.9990,0.0418) [ab]	(1.0037,0.0242) [c]	(1.0026,0.0210) [de]	(1.0131,0.2182) [d]
Changlot Real	(0.9927,0.0280) [a]	(0.9959,0.0202) [ab]	(0.9884,0.0423) [a]	(1.0054,0.0290) [cd]	(1.0008,0.0205) [cd]	(0.9941,0.0723) [d]
Lechín de Sevilla	(0.9973,0.0287) [ab]	(1.0034,0.0231) [c]	(0.9979,0.0438) [ab]	(0.9910,0.0277) [b]	(1.0085,0.0240) [e]	(1.1065,0.0916) [e]
Ocal	(0.9944,0.0282) [a]	(0.9964,0.0278) [ab]	(0.9948,0.0598) [ab]	(0.9861,0.0297) [b]	(0.9867,0.0290) [a]	(0.8983,0.0648) [b]
Picual	(0.9984,0.0235) [ab]	(1.0018,0.0235) [bc]	(1.0033,0.0436) [b]	(0.9673,0.0240) [a]	(0.9899,0.0234) [ab]	(1.1714,0.0858) [f]
Verdial de Huévar	(1.0022,0.0265) [b]	(0.9975,0.0340) [bc]	(1.0005,0.0501) [ab]	(1.0086,0.0296) [cd]	(0.9930,0.0345) [ab]	(0.9430,0.0755) [c]

Dissimilar Letters Indicate Different Statistical Means According to the Analysis of Variance Using the Tukey's Test at p<0.05

trained models to the sets of external validation, the calculation of the error metrics to assess the given different estimations showed some certain trends to be analyzed.

On the one hand, focusing on mass estimation, variety-dependent models offered, systematically and by far, lower estimation error rates than the independent ones. Actually, variety-dependent models gave $|E|$ rates per variety for mass estimation below 1% with the exception of that for Changlot Real, which reached 1.16%; the mean error $|E|$ considering all varieties as a whole was 0.49% (Table 3). The trend is also corroborated by the results registered with metrics based on accumulated error, *RMSE* and *SE*. The higher error rates for the independent approach can be explained by differences in physical characteristic features, as fruit density, stone-fresh ratio, or fat content, among others. All of them, having an evident impact on mass, may differ from one variety to another. Consequently, the slope of the lines better fitting the mass-size relationship may vary among varieties, thus explaining the poorer behavior shown by the independent approach. Studied this effect, no definitive reasons can be given to discard generic variety-independent models as a feasible tool for mass estimation, but it suggests the necessity to explore alternative approaches for its more effective implementation. To this end, a future study will explore non-linear modelling, in an attempt to achieve models able to express this mass-size variability.

Respecting size estimation, satisfying results were also found. As a reference, the mean error $|E|$ for the major and minor axis length estimation was lower than 1%, excepting for a few cases, per variety and considering all of them together (Table 4 and Table 3, respectively). Notwithstanding, despite a slightly more accurate behavior could be recognized for the variety-dependent models, this difference was so subtle that suggested further analysis in order to be more conclusive. Table 5 shows the results of the one-way analysis of variance performed per variety and model approach.

TABLE 6. Results of the study of variability of manual olive size measurement performed by three different observers. N = 900, 100 per variety, where each instance is the deviation of the three individual observations given by (36).

Variety	Major Axis		Minor Axis	
	Mean Length (mm)	SME (%)	Mean Length (mm)	SME (%)
967	15.27	1.21	13.03	1.19
1030	14.59	1.19	11.92	1.30
Arbequina	15.10	2.21	13.64	0.94
Arbosana	14.32	0.93	11.31	1.0
Changlot	20.81	0.67	14.94	0.72
Lechín	20.03	1.05	14.35	1.36
Ocal	26.00	1.38	18.96	1.96
Picual	19.68	1.06	12.93	1.27
Verdial	20.67	0.94	16.38	1.08

Generally, a higher number of classes of significance resulted from the analysis of the estimations produced by the variety-independent models for the three features. Especially relevant was this difference for the case of mass, with 2 Vs 6 classes of significance, which confirms the previous conclusions and adds strong signs of statistical consistence regarding the behavior of this set of variety-dependent models. Contrary, differences were less conclusive for the case of size estimation. This fact encouraged to study the reliability of the reference objective measurements, for the major and minor axis length, taken in laboratory by hand using a digital caliper. Indeed, there are multiple factors which potentially introduce uncertainty in the procedure, as the slight elasticity of the fruits, their ellipsoidal shape and other morphological features. Table 6 compiles the results of the variability of the manual measurements performed by three different observers for a set of 900 individuals, 100 per variety. As it can be observed, the magnitude of the found variability is comparable to the analyzed slight performance deviation between the variety-dependent and variety-independent models. As this

variability may affect model training and validation in a rather random manner, the most conservative conclusion is to consider both modelling approaches comparably valid for the case of size estimation.

V. CONCLUSIONS

The present paper proposes a new methodology for the automatic counting, and the individual mass and size estimation, of olive-fruits in digital images. All this work is intended to assess the viability of a machine vision system, aimed at improving post-harvest olive-fruit grading and classification, currently performed by rather limited mechanical methods, and to lay the basis for its implementation. Thus, the proposed imaging chamber, designed to be potentially integrated in real classification machines equipped with translucent belts, provided an efficient way to carry out the acquisition of the digital images. On the other hand, the image analysis algorithm was conceived to deal with complex situations as fruit touching, or fruit cut by the image borders. It argues for the methodology could operate under a real scenario. Regarding estimation models, and by relying on external validation results, variety-dependent models outperformed the independent ones when estimating olive mass. It indicates mass-size ratio dependence from variety. Variety-dependent models showed slightly better behavior than the variety-independent ones for size estimation, again in terms of external validation. Notwithstanding, as variability of the manual reference measurements was found to have a magnitude comparable to the performance deviation of both approaches, the most conservative conclusion is to consider them analogously valid.

A. FUTHER WORK

As detailed before, 3,600 fruits from nine different olive varieties where used to train and validate the methodology. Despite these figures, along with the obtained results, support confidence in the developed methodology, further research will include new olive-fruit varieties and samples, in order to reinforce its generalization.

On the other hand, variety-dependent models consistently and outstandingly outperformed the independent ones for the case of mass estimation, providing an overall mean error |E| of 0.49%. It indicates mass-size relationship dependence from olive variety, what encourages to explore in the future non-linear modelling for the case of independent methods, in an attempt to achieve statistical models able to express this mass-size variability.

As stated before, the image analysis algorithm was developed by using MATLAB along with the Image Processing Toolbox for prototyping purposes. Future research will also be focused on the implementation of the methodology within a framework able to satisfy real-time computation.

ACKNOWLEDGMENT

The authors would like to thank ''Cooperativa Virgen de la Oliva'', for generously offering their orchards to conduct this work.

REFERENCES

[1] P. Vossen, ''Olive oil: History, production, and characteristics of the world's classic oils,'' *Amer. Soc. Horticultural Sci.*, vol. 42, no. 5, pp. 1093–1100, 2007.
[2] J. Wang, D. Zhang, T. J. A. Farooqi, L. Ma, Y. Deng, and Z. Jia, ''The olive (Olea europaea L.) industry in China: Its status, opportunities and challenges,'' *Agrofor. Syst.*, vol. 93, no. 2, pp. 395–417, 2019.
[3] International Olive Council (IOC). (2018). *World Statistics on Production, Imports, Exports and Consumption. Word Table Olive Figures. Production*. Accessed: Jan. 8, 2019. [Online]. Available: http://www.internationaloliveoil.org/estaticos/view/132-world-table-olive-figures
[4] International Olive Council (IOC). (2018). *World Statistics on Production, Imports, Exports and Consumption. Word Olive Oil Figures. Production*. Accessed: Jan. 8, 2019. [Online]. Available: http://www.internationaloliveoil.org/estaticos/view/131-world-olive-oil-figures
[5] A. Scheidel and F. Krausmann, ''Diet, trade and land use: A socio-ecological analysis of the transformation of the olive oil system,'' *Land Policy*, vol. 28, no. 1, pp. 47–56, Jan. 2011.
[6] G. Giametta and B. Bernardi, ''Olive grove equipment technology. Straddling trees: Mechanized olive harvests,'' *Adv. Horticultural Sci.*, vol. 24, no. 1, pp. 64–70, 2010.
[7] A. H. S. Gómez, P. G. García, and L. R. Navarro, ''Elaboration of table olives,'' *Grasas y Aceites*, vol. 57, no. 1, pp. 86–94, 2006.
[8] S. Kailis and D. Harris, ''Quality and safety evaluation of processed olives,'' in *Producing Table Olives*, Collingwood, VIC, Australia: Landlinks Press, 2007, ch. 6, pp. 244–246.
[9] G. P. Moreda, J. Ortiz-Cañavate, F. J. García-Ramos, and M. Ruiz-Altisent, ''Non-destructive technologies for fruit and vegetable size determination—A review,'' *J. Food Eng.*, vol. 92, no. 2, pp. 119–136, May 2009.
[10] F. Jiménez-Jiménez, S. Castro-García, G. L. Blanco-Roldán, L. Ferguson, U. A. Rosa, and J. A. Gil-Ribes, ''Table olive cultivar susceptibility to impact bruising,'' *Postharvest Biol. Technol.*, vol. 86, pp. 100–106, Dec. 2013.
[11] V. Van Linden, N. Scheerlinck, M. Desmet, and J. De Baerdemaeker, ''Factors that affect tomato bruise development as a result of mechanical impact,'' *Postharvest Biol. Technol.*, vol. 42, no. 3, pp. 260–270, Dec. 2006.
[12] N. Kondo, ''Automation on fruit and vegetable grading system and food traceability,'' *Trends Food Sci. Technol.*, vol. 21, no. 3, pp. 145–152, Mar. 2010.
[13] M. Baigvand, A. Banakar, S. Minaei, J. Khodaei, and N. Behroozi-Khazaei, ''Machine vision system for grading of dried figs,'' *Comput. Electron. Agricult.*, vol. 119, pp. 158–165, Nov. 2015.
[14] F. S. A. Sa'ad, M. F. Ibrahim, A. Y. M. Shakaff, A. Zakaria, and M. Z. Abdullah, ''Shape and weight grading of mangoes using visible imaging,'' *Comput. Electron. Agricult.*, vol. 115, pp. 51–56, Jul. 2015.
[15] Z. Wang, K. B. Walsh, and B. Verma, ''On-tree mango fruit size estimation using RGB-D images,'' *Sensors*, vol. 17, no. 12, p. 2738, Nov. 2017.
[16] A. Mizushima and R. Lu, ''An image segmentation method for apple sorting and grading using support vector machine and Otsu's method,'' *Comput. Electron. Agricult.*, vol. 94, pp. 29–37, Jun. 2013.
[17] G. Gatica, S. Best, J. Ceroni, and G. Lefranc, ''Olive fruits recognition using neural networks,'' *Procedia Comput. Sci.*, vol. 17, pp. 412–419, Jan. 2013.
[18] S. S. Martínez, D. M. Gila, A. Beyaz, J. G. Ortega, and J. G. García, ''A computer vision approach based on endocarp features for the identification of olive cultivars,'' *Comput. Electron. Agricult.*, vol. 154, pp. 341–346, Nov. 2018.
[19] A. Beyaz, M. T. özkaya, and D. Içen, ''Identification of some spanish olive cultivars using image processing techniques,'' *Sci. Horticult.*, vol. 225, pp. 286–292, Nov. 2017.
[20] R. Diaz, L. Gil, C. Serrano, M. Blasco, E. Moltó, and J. Blasco, ''Comparison of three algorithms in the classification of table olives by means of computer vision,'' *J. Food Eng.*, vol. 61, no. 1, pp. 101–107, Jan. 2004.
[21] D. A. Puerto, D. M. M. Gila, J. G. García, and J. G. Ortega, ''Sorting olive batches for the milling process using image processing,'' *Sensors*, vol. 15, no. 7, pp. 15738–15754, Jul. 2015.
[22] J. M. Ponce, A. Aquino, B. Millán, and J. M. Andújar, ''Olive-fruit mass and size estimation using image analysis and feature modeling,'' *Sensors*, vol. 18, no. 9, p. 2930, Sep. 2018.
[23] P. Soille, *Morphological Image Analysis: Principles and Applications*, 2nd ed. Germany, Berlin: Springer, 2003.

[24] M. Sonka, V. Hlavac, and R. Boyle, "Color spaces," in *Image Processing, Analysis, and Machine Vision*, 4th ed. Belmont, CA, USA: Cengage Learning, 2014, pp. 36–38.
[25] W. Castro, J. Oblitas, M. De-la-Torre, C. Cotrina, K. Bazán, and H. Avila-George, "Classification of Cape gooseberry fruit according to its level of ripeness using machine learning techniques and different color spaces," *IEEE Access*, vol. 7, pp. 27389–27400, 2019.
[26] F. Mendoza, P. Dejmek, and J. M. Aguilera, "Calibrated color measurements of agricultural foods using image analysis," *Postharvest Biol. Technol.*, vol. 41, no. 3, pp. 285–295, 2006.
[27] N. Otsu, "A threshold selection method from gray-level histograms," *IEEE Trans. Syst., Man, Cybern.*, vol. 9, no. 1, pp. 62–66, Jan. 1979.
[28] S. Beucher and C. Lantuéjoul, "Use of watersheds in contour detection," in *Proc. Int. Workshop Image Process. Real-Time Edge Motion Detection*, Rennes, France, 1979, pp. 391–396.
[29] S. Beucher and F. Meyer, "The morphological approach to segmentation: The watershed transformation. Mathematical morphology in image processing," *Opt. Eng.*, vol. 34, pp. 433–481, 1993.
[30] F. Meyer and S. Beucher, "Morphological segmentation," *J. Vis. Commun. Image Represent.*, vol. 1, no. 1, pp. 21–46, 1990.
[31] L. Vincent, "Morphological grayscale reconstruction in image analysis: Applications and efficient algorithms," *IEEE Trans. Image Process.*, vol. 2, no. 2, pp. 176–201, Apr. 1993.
[32] A. K. Jain, "Image analysis and computer vision," in *Fundamentals of Digital Image Processing*. Englewood Cliffs, NJ, USA: Prentice-Hall, 1989, ch. 9, pp. 377–394.
[33] J. W. Tukey, "Comparing individual means in the analysis of variance," *Biometrics*, vol. 5, no. 2, pp. 99–114, Jun. 1949.

JUAN M. PONCE was born in Huelva, Andalusia, Spain, in 1982. He received the Engineer's degree in computer sciences from the University of Seville, Seville, in 2009.

After performing different jobs within the software development industry as a Programmer and Analyst, nowadays, he is with the University of Huelva, Huelva, where he is currently pursuing the Ph.D. degree in image analysis. His research is focused on developing computer-vision-based technology, potentially applicable in the food industry and precision agriculture.

ARTURO AQUINO was born in Huelva, Andalusia, Spain, in 1982. He received the M.Sc. degree in computer engineering and networks from the University of Granada, in 2007, and the Ph.D. degree in image analysis from the University of Huelva, in 2011.

He was an Engineer in computer sciences with the University of Seville, in 2006. Since 2007, he has been working in various academic posts at the University of Granada; the University of Huelva; the Research Centre for Mathematical Morphology, Mines ParisTech; and the University of La Rioja. He is currently a Postdoctoral Researcher and Lecturer with the University of Huelva. Until 2019, he has published over 40 papers, including articles, book chapters, and contributions to conferences, and holds two patents. He has directed a doctoral thesis and has participated in eight European, national, and regional research projects. His research interests include image analysis, processing, and understanding.

BORJA MILLAN was born in Zaragoza, Spain, in 1982. He received the B.S. degree in industrial engineering and the Ph.D. degree in sustainable agricultural ecosystems from the University of La Rioja, Logroño, in 2011 and 2017, respectively.

He is currently teaching and researching with the Department of Electronic Engineering, Computer Systems and Automation, University of Huelva, with a Juan de la Cierva Grant from the Spanish Ministry of Science, Innovation, and Universities. He has published over 15 publications indexed in JCR, five patents, and has worked in five European, four national, and four regional projects. He has carried out research stays at the Valencian Institute of Agrarian Research (IVIA) and at the Center for Mathematical Morphology (CMM) of the University of ParisTech. His research interests include computer vision, remote sensing, and electronics applied to precision agriculture.

Dr. Millan has received several awards and honors, including the first prize for final career projects from the College of Industrial Engineers of Aragon and La Rioja and obtained the first prize in the Business Ideas Competition from the Chair of Entrepreneurs at the University of La Rioja.

JOSÉ M. ANDÚJAR was born in Huelva, Spain. He received the Ph.D. degree from the University of Huelva, in 2000. He is currently a Full Professor of systems engineering and automatic control with the University of Huelva, Spain. He has conducted 10 Doctoral Theses with eight prizes, and holds 12 international patents. He has over 100 papers published in indexed journals in the ISI Journal Citation Reports. Specifically, he has 51 quartile Q1 publications in 20 different journals; most of these are among the top 10 in their categories, and several are number one. He has led or co-led over 50 research projects funded by public institutions and companies. His main research interests are control engineering, renewable energy systems, remote piloted aircraft systems applications, and engineering education. Throughout his professional life, he has received 24 awards and academic honors.